Nuclear Engineering and Design 428 (2024) 113470

Contents lists available at ScienceDirect

Nuclear Engineering and Design

journal homepage: www.elsevier.com/locate/nucengdes

Numerical transfer towards unresolved morphology representation in the *MultiMorph* model

Richard Meller [a,*], Benjamin Krull [a], Fabian Schlegel [a], Matej Tekavčič [b]

[a] Helmholtz-Zentrum Dresden - Rossendorf e.V., Institute of Fluid Dynamics, Bautzner Landstr. 400, 01328 Dresden, Germany
[b] Jožef Stefan Institute, Reactor Engineering Division, Jamova cesta 39, 1000 Ljubljana, Slovenia

ARTICLE INFO

Keywords:
Multiphase flows
Numerical simulation
Euler-Euler
Morphology-adaptive model

ABSTRACT

The morphology-adaptive multifield two-fluid model *MultiMorph* focuses on the reliable and robust simulation of interfacial multiphase flows in industrial applications. The idea is to combine the Volume-of-Fluid approach with the Euler-Euler approach to model both large and small scale interfacial structures efficiently. The choice of the local representation of interfacial structures, such as bubbles or droplets, by either the first or the second of the aforementioned basic method strongly depends on the ratio of the length scale of the interface feature to the grid spacing. In case the computational grid gets too coarse to locally resolve an interfacial structure, a morphology transfer is required. Such a transfer process allows to convert resolved fluid into non-resolved one, i.e. changing from a continuous description to a disperse one. A formulation for such a numerically motivated morphology transfer process is presented. It is validated with a case of a two-dimensional single rising bubble on a grid with gradually varying cell size. The model is then applied to two further cases: an oil–water phase inversion and a water jet plunging into a free water surface. Hereby, functionality, robustness and feasibility of the proposed morphology transfer mechanism are demonstrated. This work contributes to a hybrid modelling approach for the simulation of two-phase flows adapting the numerical representation depending on local flow morphology and on available computational resources.

1. Introduction

Gas-liquid multiphase flows are of great importance in a large variety of different natural flows as well as in industrial applications. The major challenge in their prediction stems from the fact that they occur on a wide range of length scales, which makes the numerical simulation difficult. Special numerical techniques are applied for different levels of spatial resolution. In recent years, efforts have been made towards hybrid multiphase models combining several specialised methods in order to cover the demand of predictive simulations with feasible computational cost. One possible choice is a Volume-of-Fluid (*VOF*) method for large scale interfacial structures in combination with the Euler-Euler model (*E-E*, also known as two-fluid model) for describing dispersed particles, bubbles or droplets, which are smaller than grid scale, in an averaged manner. Examples for such hybrid models are *GEMMA* (Colombo et al., 2022), *HD-LIS* (Frederix et al., 2021), *LIM* (Mer et al., 2018) and *MultiMorph* (formerly referred to as *OpenFOAM-Hybrid*) (Schlegel et al., 2023). In the case of large-scale interfaces, i.e. in the boundary case of an infinitely strong interfacial momentum coupling, the aforementioned models operate in a VOF-like mode. Depending on the method, this corresponds either to a single-field VOF or to a multifield VOF with individual numerical fields for phase fraction and phase-specific velocity. It has been shown that the desired VOF behaviour is recovered with the *MultiMorph* model (Meller et al., 2021).

It is a likely scenario that the size of an interfacial structure changes drastically in relation to the local grid spacing. This might happen either due to physical processes, such as entrainment or breakup, or due to local grid refinement. In any case, *morphology transfers* are necessary to transform a *continuous* phase (resolved with VOF) into *disperse* one (non-resolved with E-E) or the other way round. While those transfers are not included in *GEMMA* (Colombo et al., 2022), *HD-LIS* (Frederix et al., 2021) takes both transfer directions into account, based on the local composition of the phase mixture considering only the phase changing its morphology. The *LIM* approach (Mer et al., 2018) comes in two flavours: (a) *GLIM*, which does not explicitly account for morphology transfers similarly to *GEMMA*, and (b) *LBM*. In the latter model the transfers in both directions are considered with transfer criteria being based on the gradients of according phase fractions. For *MultiMorph* a conversion from disperse towards continuous phase fraction was

* Corresponding author.
E-mail addresses: r.meller@hzdr.de (R. Meller), b.krull@hzdr.de (B. Krull), f.schlegel@hzdr.de (F. Schlegel), matej.tekavcic@ijs.si (M. Tekavčič).

https://doi.org/10.1016/j.nucengdes.2024.113470
Received 28 March 2024; Received in revised form 9 July 2024; Accepted 11 July 2024
Available online 19 July 2024

proposed, based on the sum of the continuous and disperse volume fraction values (Krull et al., 2023). It is part of *MultiMorph* and applied hereafter.

A general overview over the features of the *MultiMorph* model is given by Schlegel et al. (2023) and the description of the basic framework and the numerical model is to be found in Meller et al. (2021). Turbulence damping is applied to the turbulence modelling of continuous phases near a large scale interface for an improved prediction of the wall-near shear layer in that region (Tekavčič et al., 2021). In case the interfacial region and the velocity gradients in the neighbouring shear layer are not sufficiently refined with the local grid resolution, a resolution-adaptive drag formulation is applied, which takes into account the type of flow structure near the interface (Meller et al., 2023). In case of high interfacial shear rate at a gas-liquid interface, droplets might be sheared of from the continuous liquid phase. In such a case the conversion from continuous to disperse liquid, i.e. liquid droplets, is described by a droplet entrainment model (Wang et al., 2023). If, for any reasons, the local grid spacing becomes small compared to the disperse phase length scale, such as droplet or bubble diameter, the Euler-Euler with its typical interfacial momentum closures is known to potentially predict nonphysically strong accumulation of disperse phase such as bubbles. In order to prevent this and to achieve grid independent behaviour in the Euler-Euler mode of the *MultiMorph* model, an explicit step of filtering is applied to the disperse phase fraction field (Krull et al., 2024). The source code of the *MultiMorph* model is public domain (Schlegel et al., 2022a). Based on these developments, a further key feature is now added to the model, namely the conversion from continuous towards disperse structures.

In the present work, a formulation for the morphology transfer from a continuous phase representation to a disperse one is proposed, allowing to adapt to insufficient spatial resolutions. This model considers both the phase volume fraction of the continuous phase and the geometry of the interface. This morphology transfer is referred to as *transfer to disperse* in the following. It is important to note, that such a morphology transfer does not only impact the choice of interfacial closure model formulation but it is also connected to a fundamental change in the representation and meaning. While dispersed structures are solved with the Euler-Euler model, they are represented statistically, meaning the resulting fields have to be interpreted as distributions of probability of the appearance of a specific phase, such as gas bubbles. Contrarily, with the Volume-of-Fluid-like approach large-scale interfaces are described via a deterministic, instant representation, i.e., the precise interface location is known (in the boundaries of the accuracy of the numerical method). By applying *transfer to disperse*, the precise knowledge about the position of interfaces is given up and is replaced with a statistical description. The loss of information connected to that needs to be compensated via a more abstract degree of modelling, which is considered via the interfacial momentum exchange models in the Euler-Euler model.

At first, in Section 2, the basic hybrid model is briefly described together with the formulation of *transfer to disperse*. Subsequently, in Section 3, the model functionality is demonstrated in a two-dimensional case of a rising gas bubble on a computational grid of varying grid spacing, in the two-dimensional case of a phase inversion of oil in viscous water, as well as in the three-dimensional simulation of a plunging water jet. Finally, in Section 4, conclusion and perspectives are given.

2. Method

2.1. Morphology-adaptive multifield two-fluid model

In the following, the numerical method will be sketched briefly. For further details the reader is referred to Meller et al. (2021). The *MultiMorph* model is based on a multifield two-fluid model formulation, meaning a unified set of balance equations is formulated individually for each combination of physical phase and morphology representation (namely continuous or disperse). An arbitrary number of phases can be described as interpenetrating continua. For each phase α the conservation equations for mass and momentum are

$$\partial_t r_\alpha \rho_\alpha + \partial_i r_\alpha \rho_\alpha u_{\alpha,i} = \sum_{\beta \neq \alpha} \Gamma^{\mathrm{PT}}_{\alpha\beta}, \tag{1}$$

$$\begin{aligned}\partial_t r_\alpha \rho_\alpha u_{\alpha,i} + \partial_j r_\alpha \rho_\alpha u_{\alpha,i} u_{\alpha,j} = &- r_\alpha \partial_i p + \partial_j 2 r_\alpha \mu_\alpha S_{\alpha,ij} + r_\alpha g_i \rho_\alpha \\ &+ \sum_{\beta \neq \alpha} r_\alpha \sigma_{\alpha\beta} \kappa_{\alpha\beta} n_{\alpha\beta,i} \\ &+ f^{\mathrm{MT}}_{\alpha,i} + \sum_{\beta \neq \alpha} \Gamma^{\mathrm{PT}}_{\alpha\beta} u_{\beta,i}.\end{aligned} \tag{2}$$

The Einstein summation convention applies for Latin indices. The time is denoted as t and indices i and j indicate spatial directions of Cartesian coordinates x, y or x, y, z in two- or three-dimensional space, respectively. The phase volume fraction of phase α is referred to as r_α, its phase specific velocity and density are denoted as $u_{\alpha,i}$ and ρ_α, respectively. The pressure p is shared between all phases. The phase specific strain-rate tensor is $S_{\alpha,ij} = 1/2\left(\partial u_{\alpha,j}/\partial x_i + \partial u_{\alpha,i}/\partial x_j\right) - 1/3\,\delta_{ij}\,\partial u_{\alpha,k}/\partial x_k$. The vector of gravitational acceleration is g_i. The symbols $\sigma_{\alpha\beta}$, $\kappa_{\alpha\beta}$ and $n_{\alpha\beta,i}$ are the surface tension coefficient between phases α and β, the curvature and the normal vector of the interface shared by those phases, respectively. The total interfacial momentum transfer acting on phase α is referred to as $f^{\mathrm{MT}}_{\alpha,i}$.

For a pair of two continuous phases, drag modelling for large scale interfaces is applied with an interfacial drag force between two phases, α and β, which are defined as

$$\mathbf{f}^D_{\alpha\beta} = K^D_{\alpha\beta}\left(\mathbf{u}_\beta - \mathbf{u}_\alpha\right). \tag{3}$$

For a well-resolved interface (R) the drag coefficient, $K^D_{\alpha\beta}$, is chosen according to Štrubelj and Tiselj (2011), such that interfacial slip is completely suppressed:

$$K^{\mathrm{D,R}}_{\alpha\beta} = r_\alpha r_\beta \frac{\rho_{\alpha\beta}}{\tau_r}, \text{with } \rho_{\alpha\beta} = \frac{r_\alpha \rho_\alpha + r_\beta \rho_\beta}{r_\alpha + r_\beta}. \tag{4}$$

The relaxation time scale, τ_r, is much smaller compared to the numerical time step size. This ensures that velocities of phases α and β are practically equal (Štrubelj and Tiselj, 2011). In *MultiMorph* the relaxation time scale is chosen to be 10^{-8} times the numerical time step size (Meller et al., 2021).

In case the shear flow in the vicinity of the interface is considered under-resolved (*UR*) interfacial slip is allowed. This is achieved by a lower drag coefficient compared to the previous drag closure model. A basic drag model (Ishii and Mishima, 1984) is chosen, which is based on a drag coefficient, C_d, which is a model parameter in addition to the interfacial area density, A_d:

$$K^{\mathrm{D,UR}}_{\alpha\beta} = r_\alpha \rho_{\alpha\beta} C_d A_d \left|\mathbf{u}_\beta - \mathbf{u}_\alpha\right|, \text{with } A_d = \frac{2\,|\nabla r_\alpha|\,|\nabla r_\beta|}{|\nabla r_\alpha| + |\nabla r_\beta|}. \tag{5}$$

The interfacial drag is then blended based on the under-resolution indicator, $\xi^{\mathrm{UR}}_{\alpha\beta}$ (Meller et al., 2023). This quantity takes a value of zero for a well-resolved interface or if a stagnation type of flow is detected in the interface region. If a fully under-resolved interfacial shear flow is detected, then $\xi^{\mathrm{UR}}_{\alpha\beta} = 1$. Additionally, values between zero and one are also allowed for intermediate degrees of resolution. The drag coefficient is then defined as

$$K^{\mathrm{D}}_{\alpha\beta} = \frac{K^{\mathrm{D,UR}}_{\alpha\beta} K^{\mathrm{D,R}}_{\alpha\beta}}{K^{\mathrm{D,UR}}_{\alpha\beta} + \xi^{\mathrm{UR}}_{\alpha\beta} K^{\mathrm{D,R}}_{\alpha\beta}}. \tag{6}$$

In the first limiting case, $\xi^{\mathrm{UR}}_{\alpha\beta} = 0$, the resolving drag coefficient $K^{\mathrm{D,R}}$ is recovered. In the second limiting case, $\xi^{\mathrm{UR}}_{\alpha\beta} = 1$, the under-resolving drag coefficient $K^{\mathrm{D,UR}}$ is effectively recovered, because $K^{\mathrm{D,UR}} \ll K^{\mathrm{D,R}}$ holds due to the extremely small relaxation time scale, τ_r. For further details the reader is referred to Meller et al. (2023). Additionally

this interface treatment is combined with an interface compression term (Weller, 2008) to counteract numerically induced diffusion of the interface.

For a pair of a disperse gas and a continuous liquid phase, the *baseline* closure model set for dispersed bubbly flows is applied (Hänsch et al., 2021). This set of closure models comprises the drag correlation of Ishii and Zuber (1979), the shear based lift correlation of Tomiyama et al. (2002), the virtual mass correction according to Crowe et al. (2012) and the correlation for wall lubrication by Hosokawa et al. (2002). Turbulence modelling is considered via the k-ω SST model (Menter et al., 2003) for the liquid phase, while disperse gas is treated as laminar phase. The turbulent dispersion of Burns et al. (2004) is used and bubble induced turbulence is accounted for via the correlation of Ma et al. (2017). The rate of interfacial phase transfer (PT) from phase β towards phase α is denoted as $\Gamma^{\mathrm{PT}}_{\alpha\beta}$.

The system of equations is solved numerically via a Finite-Volume method on unstructured grids in a segregated manner. The spatial discretisation is second-order accurate and time integration is realised semi-implicitly with first order accuracy. Transport equations for turbulent kinetic energy k and turbulent specific dissipation rate ω are spatially discretised first order accurate. Continuous phase fraction fields are sharpened in regions of large-scale interfaces via a dedicated compression term (Weller, 2008). The *MultiMorph* model is implemented as an add-on to the open-source *C++* software library by the *OpenFOAM* Foundation (The OpenFOAM Foundation Ltd) and is public domain (Schlegel et al., 2022a).

2.2. Transfer to disperse

When continuous (c) large-scale interfacial structures become too small to be resolved on the computational grid – due to physical breakup or due to a coarsening of the grid – the type of description needs to be switched towards the disperse representation (d). The mass transfer rate of this *transfer to disperse* morphology transfer is defined as

$$\Gamma^{\mathrm{PT,disint}}_{\mathrm{dc}} = \begin{cases} (1-I_{\mathrm{c}})\frac{\sqrt{r_{\mathrm{c}}}\rho_{\mathrm{c}}}{\tau} & \text{for } r_{\mathrm{c}} < r_{\mathrm{max,c}} \text{ and } \sum_{\alpha\in\mathrm{C}} r_\alpha > 0.5, \\ 0 & \text{otherwise.} \end{cases} \tag{7}$$

The symbol τ denotes a constant characteristic time scale of the morphology transfer. Currently, the time scale, τ, is a model parameter, which results to be independent from the time-step size and which has to be selected a-priori. It should best reflect the time scale, at which the bubbles approach the interface region. In that way neither gas will accumulate in the interface region, nor does the morphology transfer take place on a time scale similar to the time integration, which would lead to numerically induced artefacts. The true value of τ depends on the specific flow situation. A general approach for the determination of this parameter is highly desirable and should be focus of future endeavours. The purpose of the continuous structure indicator I_{c} is to indicate locations of large-scale interfacial structures, which are well resolved in relation to the local grid size. This is achieved by setting $I_{\mathrm{c}} = 1$, wherever $r_{\mathrm{c}} > 74\,\%$, reflecting the closest packing density of spheres. Subsequently, an additional layer with a thickness of $N_{\mathrm{c}} = 2$ grid cells, located in the direction of the negative gradient of r_{c}, is also masked with $I_{\mathrm{c}} = 1$. Everywhere else, $I_{\mathrm{c}} = 0$ applies. In that way, resolved interfaces are as reliably identified as such and, therefore, protected from being disrupted by the transfer process. With this procedure, the grid resolution is implicitly taken into account in relation to the size of the continuous structure. For instance, a gas bubble, which is coarsely resolved is characterised by an gas-liquid interface, which is smeared over a distance of the size of multiple grid cells. Note that the transfer rate is computed from the square root of the continuous phase fraction, $\sqrt{r_{\mathrm{c}}}$. The reason is the following: a source term which is linear to the changing quantity itself ($\partial_t f \sim f$) results in an exponential growth. The final value is then only reached asymptotically, i.e. never exactly. The present formulation however proposes a non-linear source term proportional to $\sqrt{r_{\mathrm{c}}}$. This produces a polynomial growth of r_{c}, the final value is reached precisely and quickly. It simplifies the numerical treatment of transfers where the continuous phase vanishes completely ($r_{\mathrm{c}} \to 0$). The first condition, $r_{\mathrm{c}} < r_{\mathrm{max,c}}$, with the maximum local volume fraction among all continuous phases, $r_{\mathrm{max,c}}$, prevents the disintegration of the dominating continuous phase. For example, continuous air should only disintegrate into disperse bubbles, if another continuous phase like water is dominantly present in that particular location. The second condition, based on the total local volume fraction of all continuous phases, $\sum_{\alpha\in\mathrm{C}} r_\alpha$, ensures the existence of a continuous phase at all. Hence, the morphology transfer is not triggered if disperse phases are dominating the phase mixture. This prevents poorly defined states, in particular the situation where only droplets and bubbles are present.

3. Results and discussion

3.1. Rising bubble

The first test case considers a two-dimensional gas bubble (G) rising in stagnant liquid (L). The basic conditions are inspired by the benchmark *Case 1* of Hysing et al. (2009). The general functionality of the numerical model in the aforementioned case has been demonstrated in a previous work (Meller et al., 2021). The gas is initialised as circular bubble of diameter $D_b = 0.5\,\mathrm{m}$. Both density and dynamic viscosity ratios of liquid to gas are $\rho_{\mathrm{L}}/\rho_{\mathrm{G}} = \mu_{\mathrm{L}}/\mu_{\mathrm{G}} = 10$. The gravitational Reynolds number is $Re_g = \rho_{\mathrm{L}} U_g D_b/\mu_{\mathrm{L}} = 35$ and the Eötvös number is $Eo = \rho_{\mathrm{L}} U_g^2 D_b/\sigma_{\mathrm{GL}} = 10$. The two latter dimensionless numbers are based on the gravitational velocity $U_g = \sqrt{g D_b}$, with the magnitude of gravitational acceleration, g. The domain is chosen to be much larger than in the original benchmark case, spanning $8D_b \times 28D_b$ in $x \times y$ directions, respectively. The origin is located in the bottom centre of the domain. The gravity is directed in negative y-direction. The initial position of the centre of gravity of the bubble is located at $(0, D_b)$. Top and bottom walls are no-slip walls for the continuous gas and liquid phases and free-slip for the disperse gas phase. The lateral boundaries act as free-slip walls for all continuous and disperse phases. For the momentum exchange between both continuous gas and liquid phases, the resolution-adaptive interfacial drag model (Meller et al., 2023) is used with a drag coefficient of $C_D = 1.6$ for the *under-resolving* drag model. The performance of this drag closure for rising gas bubbles has been demonstrated by Meller et al. (2023). The domain is discretised with an orthogonal computational grid.

To obtain a reference solution, a fine grid of 160×560 cells in $x \times y$ directions is used, resulting in a grid spacing of $0.05D_b$. The temporal evolution of the phase fraction of continuous gas, r_{c}, obtained with this grid and without the morphology transfer is presented in Fig. 1(a). Right at the beginning the gas bubble takes a flat shape, which is maintained during the time of observation ($t \leq 24\,\mathrm{s}$). It rises in a nearly straight, vertical line with equidistant vertical position changes, when observed at time intervals of 4 s.

In order to assess the *MultiMorph* model, a computational grid with locally varying grid spacing is used hereafter. Based on a background grid with 10×35 cells in $x \times y$ directions resulting in a grid spacing of $0.8D_b$, the grid cells are refined in four consecutive steps from top to bottom at the locations $y = \{20, 12, 8, 4\}D_b$ (bottom of the domain corresponds to $y = 0$). In each refinement step the grid spacing is reduced by half, resulting in a total number of 9710 grid cells. The resulting computational grid is shown in Fig. 1(b). The grid spacing in the region of highest resolution is identical to the resolution of the reference grid shown in Fig. 1(a).

At first, the dynamic of the gas bubble is investigated, predicted on that new computational grid without morphology transfer. Fig. 1(c) shows the resulting, implausible simulation results obtained if no special care is taken to address the under-resolution. In the early phase at $t = 4\,\mathrm{s}$ and 8 s, when the gas bubble travels through the region of the

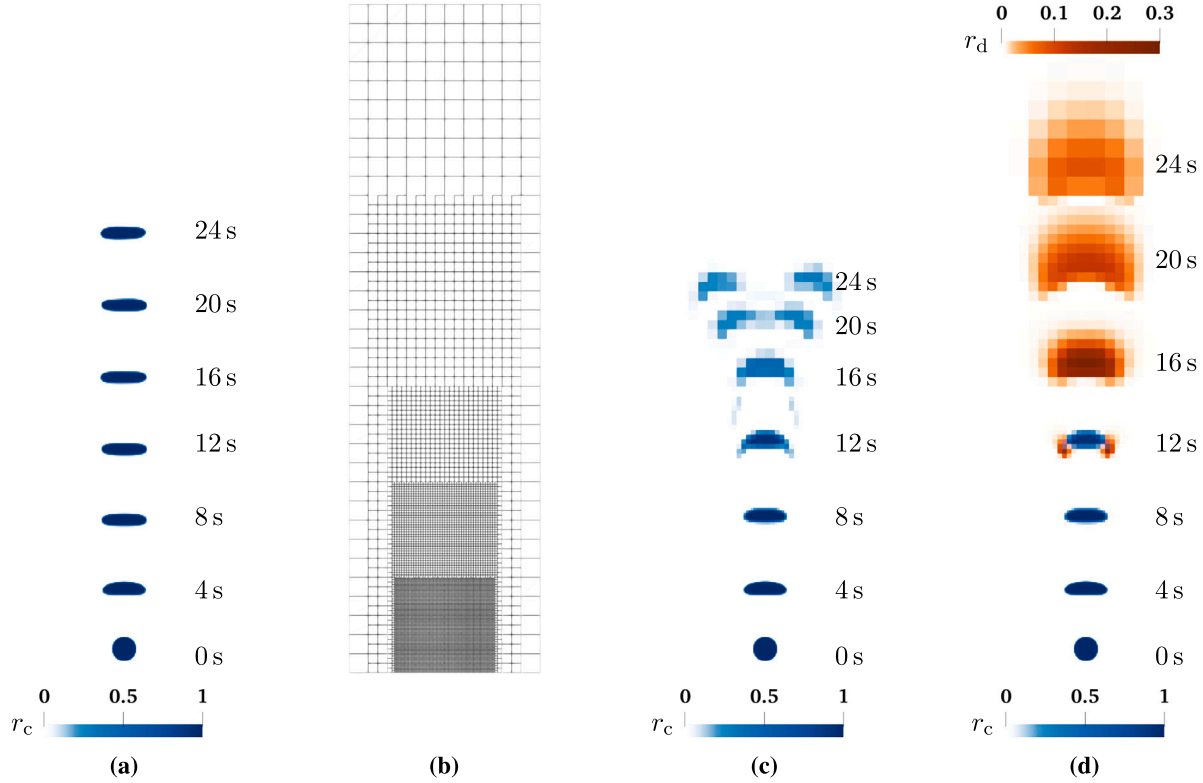

Fig. 1. Results of rising bubble case in 4 s intervals with $t \in [0, 24]$ s; (a) distribution of continuous gas (r_c, blue) obtained with fine grid for reference, (b) computational grid with locally varying grid spacing, (c) distribution of continuous gas without morphology transfer, (d) distribution of continuous and of disperse gas (r_d, orange) with *transfer to disperse*.

two finest grid resolutions, it still behaves as expected and similar to the reference data. At $t = 12$ s however, the bubble passes the region of intermediate grid resolution and the continuous gas volume fraction starts to smear out at the lateral parts of the bubble surface. As soon as the bubble reaches the second coarsest mesh region, without the morphology transfer the continuous gas structure quickly breaks up and is slowing down rapidly, even though the interface compression mechanism is active (Weller, 2008).

In order to improve the prediction, the diameter of the disperse gas for the momentum exchange modelling for (disperse) bubbly flows (Hänsch et al., 2021) is set identical to the initial diameter D_b of the continuous gas structure for this specific test case. All phases are considered laminar in this case, i.e. no turbulence model is used. The *transfer to disperse* morphology transfer model is used to convert continuous gas (c) into disperse one (d) with a time scale of $\tau = 0.5$ s. The distribution of both continuous and disperse gas, obtained with the proposed *transfer to disperse* morphology transfer model, is shown in Fig. 1(d) for several instances in time. Firstly, the transfer model remains passive, but begins to take effect at $t \approx 12$ s, starting to detect insufficient spatial resolution of the gas structure. The transfer of continuous gas towards disperse one is partially initiated at this time. In particular, at the lateral locations of the bubble interface the morphology transfer takes place at this stage. This are exactly the same locations, where a shear off of gas is observed in the simulation without morphology transfer. Right after reaching the region with the intermediate grid resolution, the whole amount of gas is rapidly transferred into disperse bubbles. This disperse bubble structure also tends to smear out over time, but this time without breakup of the gas structures leading to one single connected structure until $t = 24$ s. The numerical diffusion of the disperse gas is explained with the momentum transfer closure models acting on the gas phase. Those correlations are typically formulated assuming that bubbles are smaller than the computational grid cells, which is violated in the present case. The adaption of closure models to comparatively large gas bubbles described in the context of the E-E models shall be in the focus of future endeavours and is outside the scope of the present work. Note that in the E-E method, r_d can be interpret as a measure for the probability of the presence of gas at a certain point and time. Therefore, the exact position becomes more and more uncertain over time, which is reflected in a smearing of the phase-averaged gas fraction. While the prediction of the bubble position becomes less sharp compared to the simulation without morphology transfer, no numerically induced, erroneous breakup of the gas bubble results. In other words, the gas bubble remains a single entity but its exact position becomes less clear. Therefore, *transfer to disperse* enables the morphology-adaptive multiphase model to adapt simulation results to the given degree of locally available resolution.

The temporal evolution of the vertical position y_b and of the vertical velocity v_b of the centre of gravity of continuous and disperse gas is presented in Fig. 2. The evolution of bubble position and velocity confirms the identical behaviour of the continuous gas structure before reaching the second step of grid refinement at $y = 8D_b$ at $t \approx 10$ s. For $t < 4$ s the results also coincide with the reference data obtained with the fine grid, which is plausible, as the resolution of both grids matches in the lower part of the domain. Subsequently, on the grid with varying grid spacing, *transfer to disperse* leads to more and more continuous gas being transformed into disperse gas with similar rising velocity. The oscillations in the rising velocity of the continuous gas phase is explained with spatial resolution becoming insufficient to precisely predict the rise of the gas bubble. At $t \approx 15$ s, when the region of the next coarser grid is reached, the continuous gas without morphology transfer slows down significantly, reducing the rise of the bubble position over time. With *transfer to disperse* the whole gas amount is converted and the gas bubble now rises as disperse gas with an increased velocity compared to the reference data on the fine grid. The specific value of the rising velocity is directly dependent on the interfacial drag model formulation. Improving the bubble rising velocity in the disperse representation shall be the focus of future investigations, especially in situations arising directly from the *transfer*

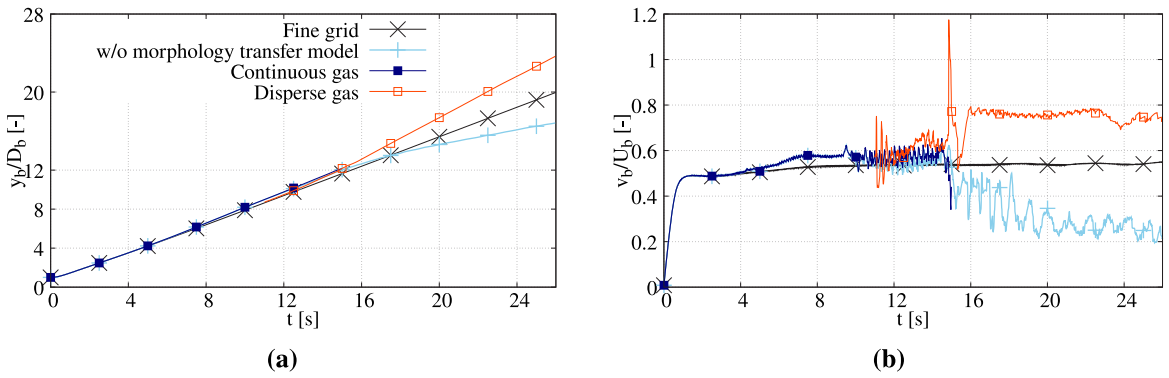

(a) (b)

Fig. 2. Evolution of centre of gravity over time for rising bubble case; (a) vertical position y_b and (b) vertical velocity component v_b; results for continuous gas r_c with and without *transfer to disperse* morphology transfer as well as for disperse gas r_d with *transfer to disperse*.

to disperse morphology transfer. Nevertheless, the velocity stays nearly constant over time, even in the region of the very coarse grid resolution.

Overall, the *transfer to disperse* morphology transfer allows for predicting a rising gas bubble without numerically induced breakup of gas structures even on very coarse computational grids. Although the rising velocity predicted for the disperse gas on the coarse grid resolution is higher than for the reference data on the fine grid, the qualitative behaviour of the gas bubble is improved compared to the simulation without morphology transfer.

3.2. Phase inversion

The second test case considers a two-dimensional phase inversion of oil (O) and viscous water (W) as proposed by Labourasse et al. (2007). The square domain with an edge length of 1 m is initially filled with water except for the lower left quarter, where slightly lighter oil is located, hence, forming an unstable configuration due to buoyancy. Oil and water have phase-specific densities of $\rho_O = 900\,\mathrm{kg\,m^{-3}}$ and $\rho_W = 1000\,\mathrm{kg\,m^{-3}}$, respectively. The phase-specific dynamic viscosities of both fluids are $\mu_O = 1 \times 10^{-1}\,\mathrm{kg\,m^{-1}\,s^{-1}}$ and $\mu_W = 5 \times 10^{-3}\,\mathrm{kg\,m^{-1}\,s^{-1}}$, respectively. The surface tension coefficient is $\sigma_{OW} = 0.045\,\mathrm{N\,m^{-1}}$ and the gravitational acceleration has a magnitude of $g = 9.81\,\mathrm{m\,s^{-2}}$. The disperse oil droplets are coupled to the water via the drag correlation of Schiller and Naumann (1933) with a modelled droplet diameter of $D_d = 4.6 \times 10^{-3}$m, corresponding to a critical Weber number of $We_{\mathrm{crit}} = 10$ (Ménard et al., 2007) based on a gravitational velocity of $U_g = 0.99\,\mathrm{m\,s^{-1}}$ (Labourasse et al., 2007). No further interfacial momentum transfer mechanisms are taken into account to describe the disperse droplet flow. All phases are considered laminar, i.e. no turbulence modelling is applied in this case. For the large-scale interface between continuous oil and water the no-slip drag correlation of Štrubelj and Tiselj (2011) is imposed. The time scale for the *transfer to disperse* morphology transfer is, again, chosen as $\tau = 0.5$ s. All four boundaries are treated as no-slip walls for all continuous and disperse phases. The domain is spatially discretised with an equidistant orthogonal grid of 64×64 grid cells. For comparison, the reference data (Labourasse et al., 2007) are obtained on a finer grid with 256×256 grid cells.

The distribution of continuous and disperse oil is presented in Fig. 3 for several instances in time. For each time instant the high-resolution reference data (256×256 grid) is shown on the left-hand side next to the simulation results obtained on the coarser grid (64×64) without morphology transfer in the centre. The results achieved on the coarse grid with *transfer to disperse* are presented on the right-hand side. The identical initial distribution for all simulations at $t = 0$ s is shown in Fig. 3(a). At first, as long as primarily continuous oil is present for $t \leq 1$ s (Fig. 3(b)), similar dynamics are observed between both cases with and without morphology transfer. At $t = 2.25$ s (Fig. 3(c)) a small amount of oil has already been transformed by *transfer to disperse*, especially right next to the left wall and at the vortex in the centre left region. At $t = 4.5$ s (Fig. 3(d)) the overall oil distribution is still similar between both setups, with and without the transfer mechanism. With the morphology transfer, however, the continuous oil is accompanied by disperse oil, mostly in the vicinity of the large scale interface region in the centre right region of the domain. In both simulations a larger portion of continuous oil starts gathering underneath the top wall due to buoyancy effects. While the overall distribution of oil is still similar at $t = 6.25$ s (Fig. 3(e)) between both cases, the continuous oil becomes more and more fragmented without the morphology transfer forming rather large fragments of oil. With *transfer to disperse* those fragments quickly become transformed and, hence, disperse oil is accumulating over time representing rather small oil droplets according to the selected modelling diameter D_d. This is in accordance with the reference of Labourasse et al. (2007), which shows a large amount of small oil droplets already at this stage of the simulation. At $t = 9.75$ s (Fig. 3(f)) a chunk of continuous oil is still observed in both setups, which gradually becomes transformed to disperse oil by *transfer to disperse*. Hence, a large cloud of droplets is formed over time. Without the morphology transfer, submerged bits of continuous oil accumulate in the water. In the reference further disintegration of oil droplets has taken place until this point in time. This can be predicted with the morphology-adaptive with *transfer to disperse*, while the approach without this morphology transfer cannot reproduce such small structures due to the limited spatial resolution. At $t = 22.25$ s (Fig. 3(g)) the oil droplets started to rise according to the reference due to buoyancy leaving behind a region of nearly pure water in the bottom centre region of the domain. The simulation without morphology transfer still shows oil structures being distributed over the whole water volume at this point. At the same time a larger accumulation of oil is observed in the simulation results with and without *transfer to disperse*. However, the results obtained with morphology transfer show that the disperse oil structures are gathered around the larger oil accumulation and on the bottom left region of the water volume no oil is observed anymore. At $t = 34.75$ s (Fig. 3(h)) the large oil accumulation observed in the present simulations has completely disintegrated, with and without morphology transfer. The small oil droplets observed in the reference data are further rising to the water–oil interface, while the latter becomes more and more smooth. While the result obtained without morphology transfer still shows a lot of oil being submerged in the water at this point, the disperse oil droplets generated by the *transfer to disperse* are steadily rising towards the large-scale interface. A lot of those fragments are still observed without the morphology transfer at $t = 42.25$ s (Fig. 3(i)). At this instance in time with *transfer to disperse* nearly the whole amount of (disperse) oil already floated to the surface and has been transformed back to continuous oil via the morphology transfer in the opposite direction (Krull et al., 2023). Only a very small amount of disperse oil is left in the water at that time, continuing to rise towards the surface, which is inline with the reference data. Also the interface becomes smooth and increasingly settled, which is close to

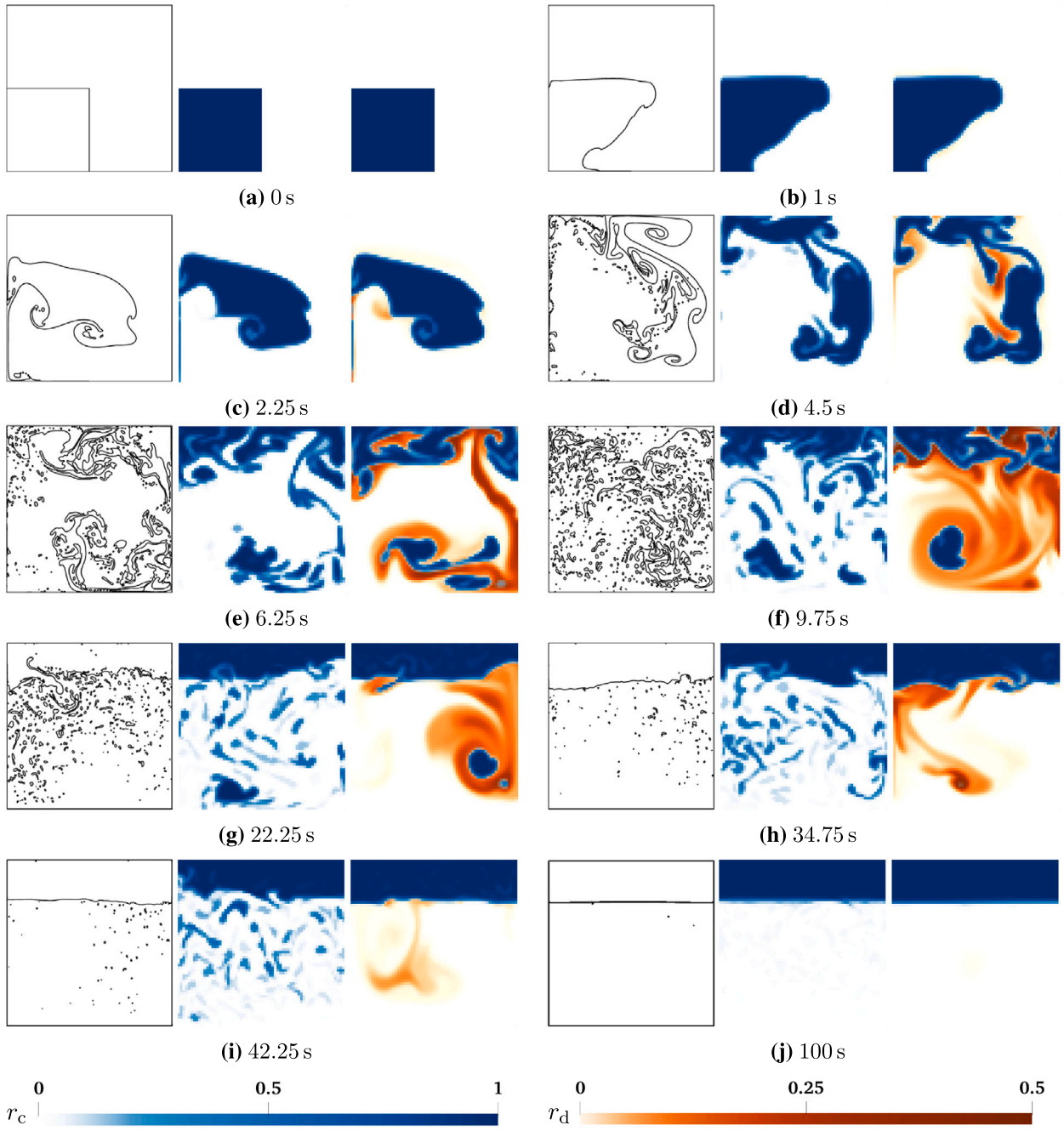

Fig. 3. Position of interface (black line) and distribution of continuous oil (r_c, blue) and disperse oil (r_d, orange) volume fraction for several instances in time for the phase inversion case; three results are shown for several instances in time — left: reference results of Labourasse et al. (2007), centre: present results obtained without morphology transfer, right: present results obtained with *transfer to disperse*.

the reference data. The simulation without morphology transfer still shows a disturbed oil–water interface at this time. Finally, at $t = 100\,\mathrm{s}$ (Fig. 3(j)) the flat interface seen in the reference data is recovered with the simulation with morphology transfer, while no submerged oil droplets are observed any more. Both immiscible liquid phases have finally segregated. This is the case for the simulation without morphology transfer, although the interface is still not perfectly flat, and small disturbances are still observed. Overall, compared to the high-resolution reference data (Labourasse et al., 2007), the interface location evolves very similar at the beginning of the simulation, both with and without morphology transfer. Describing the oil purely as a continuous phase leads to disintegration of the structures into rather large oil fragments, which are much larger than suggested by the reference data and still exist at the final time instance. Contrarily, the application of the morphology transfer model results in a very small amount of smoothly dispersed oil, reaching the stagnant stratification in accordance with the reference data at $t = 100\,\mathrm{s}$.

In order to assess the dynamics in a more quantitative manner, simulation results are compared to the reference data (Labourasse et al., 2007) in terms of the interfacial area density IAD and of the volume ratio R_V. For the continuous oil IAD is evaluated as the integral surface area of the actual oil–water interface ($r_c = 0.5$), while the quantity is calculated for the disperse oil as $\mathrm{IAD_d} = 4\,r_d/D_d$ in two-dimensional space. The volume ratio R_V is defined as the integral volume of oil in the upper quarter of the domain normalised by the volume of the whole domain. The evolution of both quantities, IAD and R_V, over

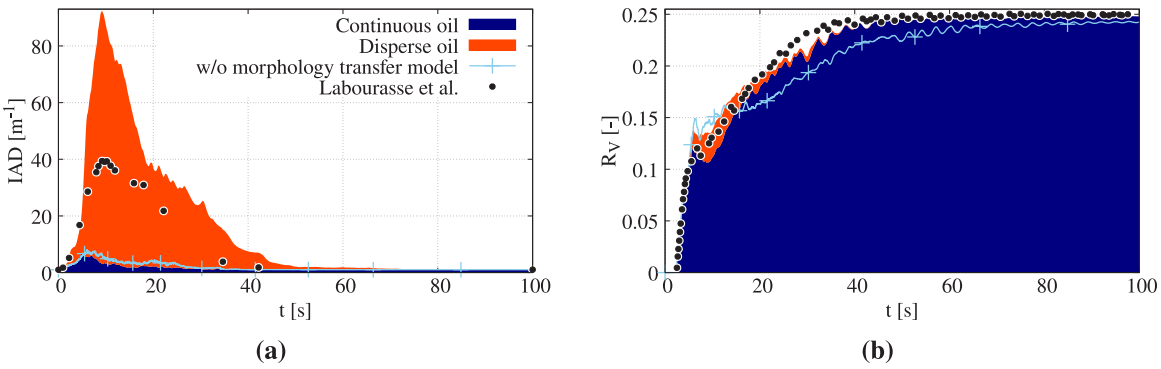

Fig. 4. Evolution of integral quantities in phase inversion case over time; (a) interfacial area density IAD, (b) volume ratio R_V; results for continuous oil with and without *transfer to disperse* morphology transfer and for disperse oil in comparison to reference data of Labourasse et al. (2007).

time for continuous oil with and without *transfer to disperse* as well as for disperse oil is presented in Fig. 4. The interfacial area density of the continuous oil shows a slight increase in the first 5 s of the simulation and subsequently decays over a period of roughly 10 s, which is observed similarly in both cases, with and without *transfer to disperse*. However, for the disperse oil IAD_d rises more rapidly until $t \approx 10$ s with a peak value of almost 90 m^{-1} before it slowly decays as well. Compared to the reference data, which show a peak value of around 40 m^{-1} the combined interfacial area density for both continuous and disperse oil is much higher, which is closely connected to the choice of the modelled droplet diameter D_d. A better model prediction of D_d, i.e. via coupling of *MultiMorph* to the population balance method (Lehnigk et al., 2021), would help to improve the results in terms of interfacial area density. Such a coupling is focus of future endeavours. However, without the morphology transfer the quantity is significantly under-predicted.

Considering the reference data the volume ratio R_V rapidly rises starting at $t \approx 3$ s, when a large portion of the oil is initially entering the upper quarter of the domain. After a slight dip the quantity rises more slowly until it nearly reaches its theoretical maximum of 0.25 at $t \approx 40$ s. Finally, R_V asymptotically grows towards the latter value with showing slight oscillations, which corresponds to the wavy motion of the oil–water interface. In the simulation results with and without morphology transfer the rapid initial rise of R_V is recovered for the continuous oil. Also the dip followed by the slow growth of the volume ratio is qualitatively observed with both setups. With *transfer to disperse* R_V of the disperse oil is appearing after the dip but it is soon fading out afterwards due to the morphology transfer in the opposite direction (Krull et al., 2023). However, the overall evolution of the volume ratio is comparatively similar to the reference data almost reaching the maximum value of 0.25 shortly after $t = 40$ s. In contrast, the simulation without morphology transfer predicts a very slow increase of R_V after the dip resulting in a value at $t = 100$ s, which is significantly lower than 0.25. In terms of the volume ratio *transfer to disperse* significantly improves the overall dynamics in the phase inversion case.

Additionally, the evolution of the kinetic energy E_{kin} integrated over the domain for the oil phase(s) resulting from both setups is compared to the reference data (Labourasse et al., 2007), which is presented in Fig. 5. In the reference data a rapid initial rise of E_{kin} is observed, followed by a fast drop. Both aforementioned features are reproduced with and without the morphology transfer. Afterwards, a second peak occurs in the reference data, which is similarly large as the first one with a peak value of $E_{kin} \approx 11.5$ J. While a second energy peak is reproduced in the present simulations, its value is overestimated without the morphology transfer with $E_{kin} \approx 14$ J, while the peak predicted with *transfer to disperse* reveals an even larger peak value of $E_{kin} \approx 16$ J. It is assumed, that the rapid disintegration of oil droplets in this early stage of the simulation observed in the reference data helps to dissipates the energy, which in turn prevents such a high peak of kinetic energy. For sure these small-scale dynamics cannot be resolved on the coarse grid used in the present simulations. However, the *transfer to disperse* morphology transfer seems to predict too little disintegration of oil droplets in this initial phase. Nevertheless, throughout the remaining simulation period, the decay of kinetic energy observed in the reference data is qualitatively reproduced both with and without morphology transfer. Without the latter the kinetic energy decays significantly slower, while *transfer to disperse* results in integral values of E_{kin}, which are similar to the reference data. This is especially observed for $t > 40$ s with the logarithmic scaling in Fig. 5(b).

Altogether, the morphology transfer itself as well as the resulting presence of the disperse oil seem to dampen the motion of the oil–water mixture dissipating kinetic energy and, hence, improving the prediction of dynamics in the phase inversion case.

3.3. Plunging jet

The third case considers a vertical water jet in air plunging onto a free surface, proposed by Chanson et al. (2004) as case *M1*. The three-dimensional domain features the same dimensions as the experiment: a diameter of 0.6 m and a total height of 1.8 m. The opening of the inlet pipe is located 0.2 m below the top boundary of the domain and the water level is initialised 1.5 m above the bottom of the domain. At the inlet, pure water is injected with a vertical velocity of 3.853 m s^{-1} through the circular inlet boundary, which has a diameter of 25 mm. An outflow is imposed at the bottom boundary, which matches the volume flow rate of the inlet in order to conserve the total volume of water within the domain. The top boundary is modelled as atmospheric boundary condition allowing back-flow of pure continuous air. The bounding surface of the cylindrical domain as well as the outer wall of the inlet pipe are modelled as no-slip walls for continuous water and air and as free-slip walls for disperse air bubbles. The air bubbles are modelled as disperse phase with the full *baseline* model set (Hänsch et al., 2021), assuming a bubble diameter of $D_b = 3.5$ mm. Turbulence is taken into account as described in Section 2.1. The momentum exchange between continuous air and water is realised by the resolution adaptive drag model (Meller et al., 2023). The time scale for the *morphology transfer to disperse* is set to $\tau = 0.1$ s.

In order to assess the influence of the spatial resolution, three different computational grids are used: coarse, medium and fine resolution grids, referred to as G1, G2 and G3, respectively (Fig. 6, top row). The computational grids consist of orthogonal cells in the centre of the cylindrical domain, with an attached O-type grid in the radial outward direction. The cell spacing is increased in the outer region. Towards both bottom and atmospheric boundaries the vertical grid spacing gradually increases. The inlet diameter is mapped with 1, 2 and 4 cells for grids G1, G2 and G3, respectively. This results in a total number of 5454, 35 776 and 277 872 grid cells, respectively.

Numerical results for the distribution of continuous air and disperse air are presented in Fig. 6. The results are temporally averaged for a

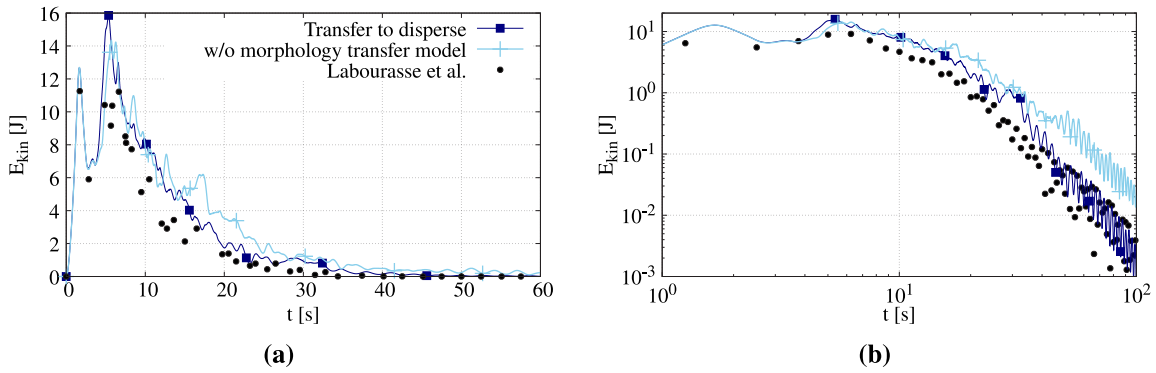

Fig. 5. Kinetic energy of oil integrated over domain with and without *transfer to disperse* morphology transfer compared to reference data of Labourasse et al. (2007); (a) linear scale, (b) logarithmic scale; results obtained with morphology transfer are presented as combined integral kinetic energy for continuous and disperse oil.

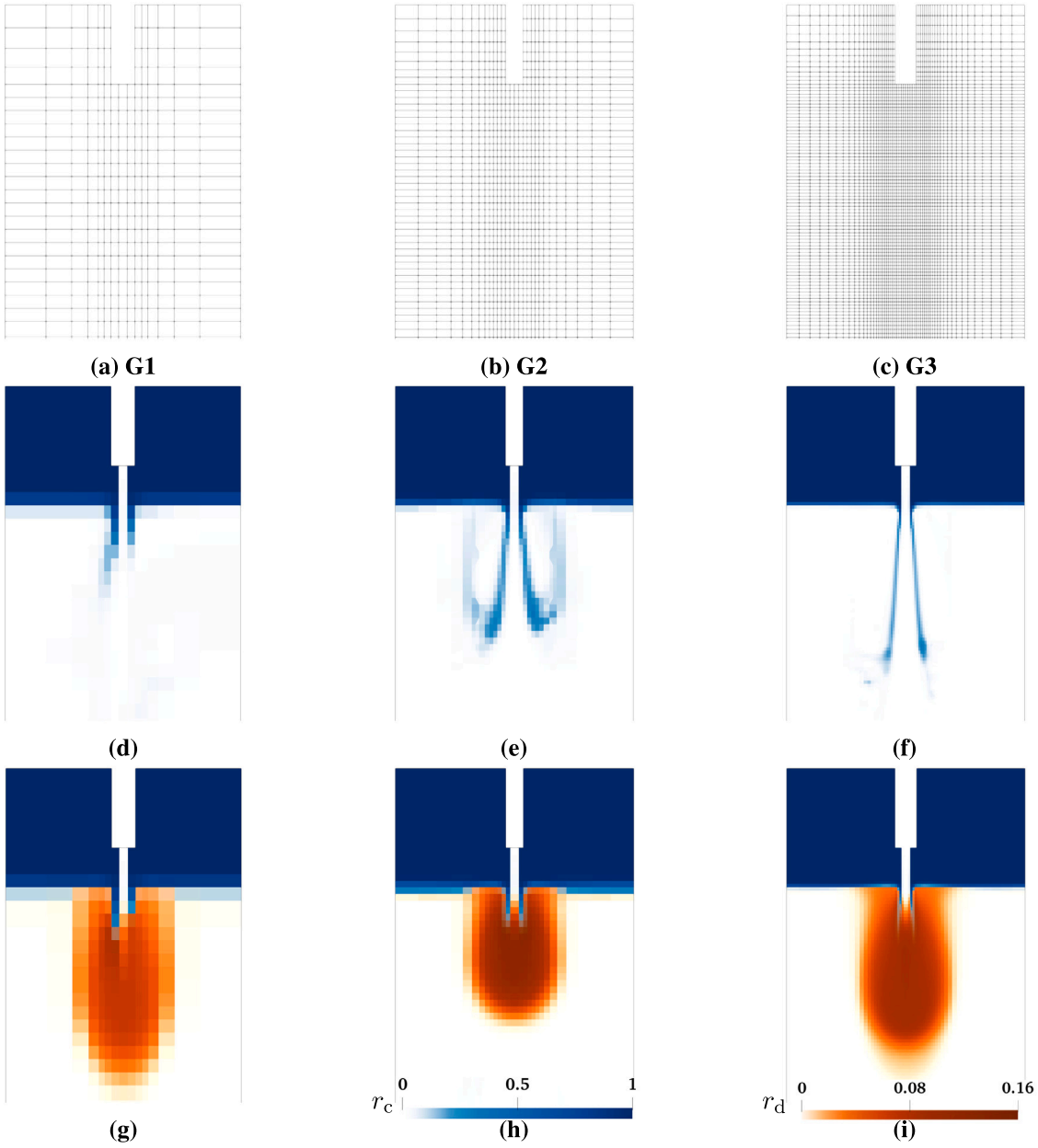

Fig. 6. Vertical cut through plunging jet case. Top row, from left to right: computational grids G1, G2, G3; centre row: time averaged distribution of continuous gas (r_c, blue) obtained without morphology transfer; bottom row: time averaged distribution of continuous gas (r_c, blue) and disperse gas (r_d, orange) obtained with *morphology transfer to disperse*.

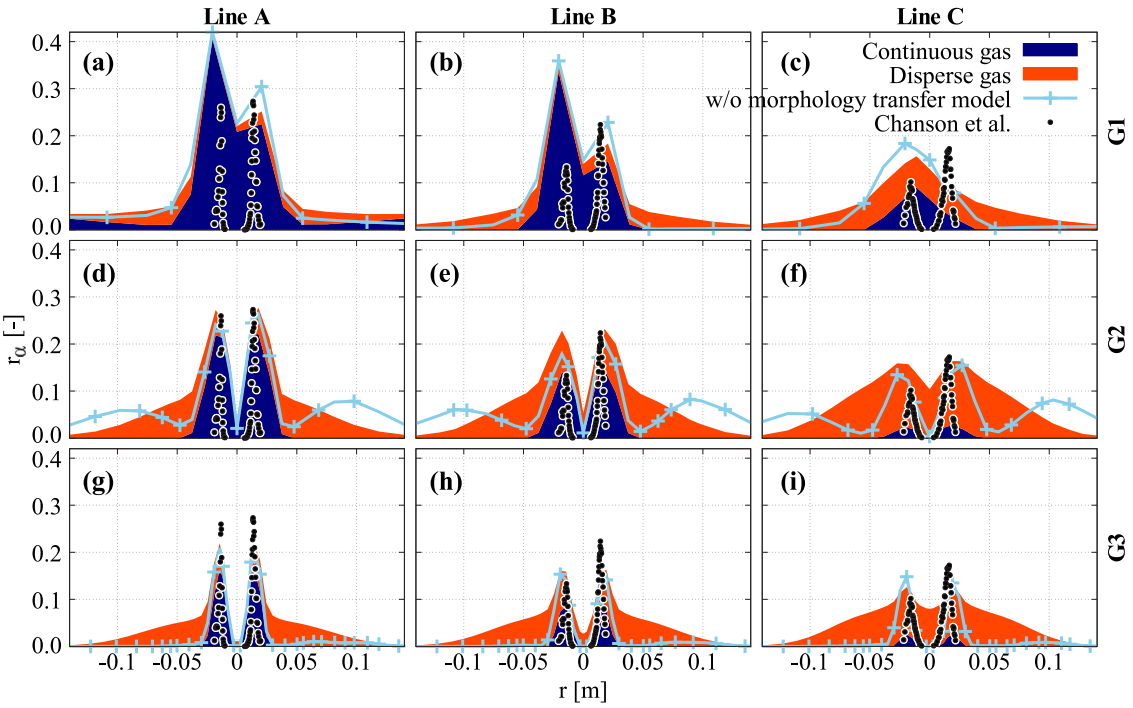

Fig. 7. Distribution of temporally averaged gas fraction along horizontal line *A* (left column), line *B* (centre column) and line *C* (right column); results are presented for computational grids G1 (top row), G2 (centre row) and G3 (bottom row); experimental data of Chanson et al. (2004) are shown for reference.

time period of $t = 5\,\mathrm{s}$ to $10\,\mathrm{s}$. Without morphology transfer, the air becomes very diffuse shortly after being entrained into the water on the coarse grid (Fig. 6(d)). With the finer grids, a thin cone of continuous air forms a pronounced plunging zone (Figs. 6(e) and 6(f)). Its shape and vertical extension strongly depends on the spatial resolution. If the morphology transfer is applied, the results change significantly: Almost no continuous air is submerged in the water, especially in deeper locations. There, all continuous air has become transformed into disperse one forming a compact cloud of air bubbles. That behaviour is observed on all three grids under investigation (Figs. 6(g), 6(h) and 6(i)). The vertical extension of the disperse air plume varies slightly with the spatial resolution, while the qualitative behaviour is the same across all grids.

For a more quantitative assessment, the radial distribution of the time averaged distribution of continuous and of disperse gas are compared to experimental measurements reported by Chanson et al. (2004). Data are extracted at three horizontal lines: line *A*, *B* and *C* located 1.46 m, 1.44 m and 1.40 m above the bottom of the domain, respectively. The gas distributions for all three computational grids are presented in Fig. 7.

Two sharp peaks are observed in the gas fraction profiles of the reference data (see for example Fig. 7a–c). The peaks are asymmetric at lines *B* and *C* with a tendency towards the right hand side (Figs. 7b and 7c). Generally, less air is observed in greater depth below the water surface (decreasing amplitude in Fig. 7a–c). It is conceivable, that bubbles rising upwards in the vicinity of the jet were not fully captured by the experiment, because there should exist at least a certain amount of gas aside from the recorded central peaks. At the coarse grid G1, the two asymmetrical gas fraction peaks are recovered at lines *A* and *B* (Figs. 7a and 7b), while at *C* a single peak is observed left to the vertical centre line (Fig. 7c). At positions *A* and *B*, the gas fraction is over-predicted by the larger of the two peaks. At *A*, the continuous gas is present everywhere and is accompanied by a small amount of disperse gas (Fig. 7a). With increasing depth (positions *B* and *C*), the continuous gas disappears from the lateral positions $r > 0.05\,\mathrm{m}$, due to the morphology transfer turning it into disperse gas. On the intermediate grid G2, both gas fraction peaks are sharper compared to G1 due to the higher spatial resolution (Fig. 7d–f). An asymmetry is not observed anymore. At line *A*, the peak values of the combined gas fraction are very close to the experimental values (Fig. 7d). At *B* and *C* the maximum combined gas fraction values are in accordance with the larger peak of the reference data (Figs. 7e and 7f). Generally, continuous gas is only present close to the peak regions in the centre of the domain, while disperse gas is present everywhere, which is most likely not measured in the experiments. With increasing radial distance, the disperse gas fraction gradually reduces and nearly reaches zero at $|r| \approx 0.15\,\mathrm{m}$ (approx. half domain radius). The simulation results without morphology transfer in Fig. 7d–f reveals gas fraction peak values at the same location but with lower values compared to the results obtained with *transfer to disperse*. At all vertical locations, additional flat gas fraction peaks are observed at $|r| \approx 0.1\,\mathrm{m}$. This observation is in accordance with the air rising towards the water surface as shown in Fig. 6(e). With the fine grid G3 (Fig. 7g–i), the gas fraction peaks are symmetrical and become even sharper and their width is now comparable to the experimental reference data. However, the peak values are lower compared to the coarser grids at all locations, *A*, *B* and *C*. While being under-predicted at line *A*, the peak values of the combined gas fraction are slightly higher than the lower peak of the experimental values (Figs. 7h and 7i). The continuous phase is purely observed at the sharp peaks, which is in accordance to the reference data. As observed with the intermediate grid, G2, disperse gas is located in a larger region around the centre and gradually reduces with increasing radial distance. However, the overall amount of disperse gas is reduced compared to the coarser grids. The results obtained without morphology transfer show only the two gas fraction peaks (Fig. 7g–i). At locations *A* and *B*, the peak values are slightly lower compared to the combined gas fraction of the morphology-adaptive model, while revealing slightly higher values at line *C*. Contrary to grid G2, only a very small amount of gas is observed at $r \approx 0.1\,\mathrm{m}$.

Overall, the *morphology transfer to disperse* reveals a more consistent behaviour across several degrees of spatial resolution, which is an improvement in comparison to the simulation without morphology transfer. However, the absolute values of gas fraction are similar among

both approaches. The major difference is observed in the distribution of the (disperse) gas bubbles, which are finally rising to the water surface. This feature cannot be assessed as it is not available in the reference data.

4. Conclusion and perspectives

Morphology-adaptive multifield two-fluid models, such as *MultiMorph*, combine VOF and E-E approaches. Such methods require to handle the transfer of phase fraction from a continuous morphology to a disperse one and vice versa. In the present work a transfer formulation called *transfer to disperse* is proposed, turning continuous phase fraction into disperse one. This extends the capability of the *MultiMorph* model (Schlegel et al., 2023). The functionality of the proposed formulation is demonstrated in three different test cases: 1. a two-dimensional gas bubble rising in stagnant liquid in a domain discretised with a locally varying grid spacing, 2. a two-dimensional phase inversion of oil and viscous water, and 3. a three-dimensional plunging water jet in ambient air. In all three cases an improvement of results is achieved compared to the simulation on coarse meshes without morphology transfer, resulting in a consistent model behaviour even with varying spatial resolution. Moreover, the dynamics of the interfacial flows are predicted more precisely.

Future endeavours might focus on the validation of the proposed transfer model for the morphology transfer of continuous liquid phases to disperse liquid phases inside a gaseous fluid. Furthermore, it is desirable to find a suitable analytical expression for the transfer time scale τ based on material properties of the liquid. In that way the case specific choice of this quantity would become superfluous. Another possible improvement would be to derive the modelled diameter from the current flow situation, potentially combined with polydisperse modelling approaches. Additionally, the proposed morphology transfer formulation might be combined with an explicit model for the entrainment of bubbles or droplets at large-scale interfaces, which takes place on length scales much smaller than the grid spacing. For this purpose the entrainment model proposed by Ma et al. (2011) shall be considered.

CRediT authorship contribution statement

Richard Meller: Writing – review & editing, Writing – original draft, Visualization, Software, Methodology, Conceptualization. **Benjamin Krull:** Writing – review & editing, Writing – original draft, Software, Methodology, Conceptualization. **Fabian Schlegel:** Writing – review & editing, Writing – original draft, Supervision, Software, Project administration, Methodology, Funding acquisition, Conceptualization. **Matej Tekavčič:** Writing – review & editing, Writing – original draft, Methodology, Conceptualization.

Declaration of competing interest

The authors declare that they have no known competing financial interests or personal relationships that could have appeared to influence the work reported in this paper.

Data availability

Data will be made available on request.

Acknowledgements

This work was supported by the Helmholtz European Partnering Program in the project *Crossing borders and scales* (Crossing). The author from the Jožef Stefan Institute gratefully acknowledges also the financial support provided by the Slovenian Research and Innovation Agency through the grant P2-0026.

References

Burns, A.D., Frank, T., Hamill, I., Shi, J.-M., 2004. The favre averaged drag model for turbulent dispersion in Eulerian multi-phase flows. In: 5th International Conference on Multiphase Flow, ICMF, vol. 4, ICMF Japan, pp. 1–17.

Chanson, H., Aoki, S., Hoque, A., 2004. Physical modelling and similitude of air bubble entrainment at vertical circular plunging jets. Chem. Eng. Sci. 59 (4), 747–758. http://dx.doi.org/10.1016/j.ces.2003.11.016.

Colombo, M., De Santis, A., Hanson, B.C., Fairweather, M., 2022. Prediction of horizontal gas–liquid segregated flow regimes with an all flow regime multifluid model. Processes 10 (5), 920. http://dx.doi.org/10.3390/pr10050920.

Crowe, C.T., Schwarzkopf, J.D., Sommerfeld, M., Tsuji, Y., 2012. Multiphase Flow with Droplets and Particles, Second ed. CRC Press, p. 509.

Frederix, E.M.A., Dovizio, D., Mathur, A., Komen, E.M.J., 2021. All-regime two-phase flow modeling using a novel four-field large interface simulation approach. Int. J. Multiph. Flow 145, 103822. http://dx.doi.org/10.1016/j.ijmultiphaseflow.2021.103822.

Hänsch, S., Evdokimov, I., Schlegel, F., Lucas, D., 2021. A workflow for the sustainable development of closure models for bubbly flows. Chem. Eng. Sci. 244, 116807. http://dx.doi.org/10.1016/j.ces.2021.116807.

Hosokawa, S., Tomiyama, A., Misaki, S., Hamada, T., 2002. Lateral migration of single bubbles due to the presence of wall. In: Fluids Engineering Division Summer Meeting, vol. 36150, pp. 855–860. http://dx.doi.org/10.1115/FEDSM2002-31148.

Hysing, S., Turek, S., Kuzmin, D., Parolini, N., Burman, E., Ganesan, S., Tobiska, L., 2009. Quantitative benchmark computations of two-dimensional bubble dynamics. Internat. J. Numer. Methods Fluids 60 (11), 1259–1288. http://dx.doi.org/10.1002/fld.1934.

Ishii, M., Mishima, K., 1984. Two-fluid model and hydrodynamic constitutive relations. Nucl. Eng. Des. 82, 107. http://dx.doi.org/10.1016/0029-5493(84)90207-3.

Ishii, M., Zuber, N., 1979. Drag coefficient and relative velocity in bubbly, droplet or particulate flows. AIChE J. 25 (5), 843–855. http://dx.doi.org/10.1002/aic.690250513.

Krull, B., Lucas, D., Meller, R., Schlegel, F., Tekavčič, M., 2023. The morphology adaptive multifield solver OpenFOAM-Hybrid and its application to multiphase flow problems in nuclear safety. In: CFD4NRS-9.

Krull, B., Meller, R., Tekavčič, M., Schlegel, F., 2024. A filtering approach for applying the two-fluid model to gas-liquid flows on high resolution grids. Chem. Eng. Sci. 290, 119909. http://dx.doi.org/10.1016/j.ces.2024.119909.

Labourasse, E., Lacanette, D., Toutant, A., Lubin, P., Vincent, S., Lebaigue, O., Caltagirone, J.-P., Sagaut, P., 2007. Towards large eddy simulation of isothermal two-phase flows: Governing equations and a priori tests. Int. J. Multiph. Flow 33 (1), 1–39. http://dx.doi.org/10.1016/j.ijmultiphaseflow.2006.05.010.

Lehnigk, R., Bainbridge, W., Liao, Y., Lucas, D., Niemi, T., Peltola, J., Schlegel, F., 2021. An open-source population balance modeling framework for the simulation of polydisperse multiphase flows. AIChE J. 68 (3), http://dx.doi.org/10.1002/aic.17539.

Ma, J., Oberai, A.A., Drew, D.A., Lahey, Jr., R.T., Hyman, M.C., 2011. A comprehensive sub-grid air entrainment model for RaNS modeling of free-surface bubbly flows. J. Comput. Multiph. Flows 3 (1), 41–56. http://dx.doi.org/10.1260/1757-482X.3.1.41.

Ma, T., Santarelli, C., Ziegenhein, T., Lucas, D., Fröhlich, J., 2017. Direct numerical simulation–based Reynolds-averaged closure for bubble-induced turbulence. Phys. Rev. Fluids 2 (3), 034301. http://dx.doi.org/10.1103/PhysRevFluids.2.034301.

Meller, R., Schlegel, F., Lucas, D., 2021. Basic verification of a numerical framework applied to a morphology adaptive multi-field two-fluid model considering bubble motions. Internat. J. Numer. Methods Fluids 93 (3), 748–773. http://dx.doi.org/10.1002/fld.4907.

Meller, R., Tekavčič, M., Krull, B., Schlegel, F., 2023. Momentum exchange modelling for coarsely resolved interfaces in a multifield two-fluid model. Internat. J. Numer. Methods Fluids 95 (9), 1521–1545. http://dx.doi.org/10.1002/fld.5215.

Ménard, T., Tanguy, S., Berlemont, A., 2007. Coupling level set/VOF/ghost fluid methods: Validation and application to 3D simulation of the primary break-up of a liquid jet. Int. J. Multiph. Flow 33 (5), 510–524. http://dx.doi.org/10.1016/j.ijmultiphaseflow.2006.11.001.

Menter, F.R., Kuntz, M., Langtry, R., 2003. Ten years of industrial experience with the SST turbulence model. Turbul. Heat Mass Transf. 4, 625–632.

Mer, S., Praud, O., Neau, H., Merigoux, N., Magnaudet, J., Roig, V., 2018. The emptying of a bottle as a test case for assessing interfacial momentum exchange models for Euler–Euler simulations of multi-scale gas-liquid flows. Int. J. Multiph. Flow 106, 109–124. http://dx.doi.org/10.1016/j.ijmultiphaseflow.2018.05.002.

Schiller, L., Naumann, A., 1933. Über die grundlegenden Berechnungen bei der Schwerkraftaufbereitung. VDI Zeitung 77 (12), 318–320.

Schlegel, F., Bilde, K.G., Draw, M., Evdokimov, I., Hänsch, S., Kamble, V.V., Khan, H., Krull, B., Lehnigk, R., Li, J., Lyu, H., Meller, R., Petelin, G., Kota, S.P., Tekavčič, M., 2022a. HZDR multiphase Addon for OpenFOAM. http://dx.doi.org/10.14278/rodare.1877, Ver. 10-s.1-hzdr.2.

Schlegel, F., Meller, R., Krull, B., Lehnigk, R., Tekavčič, M., 2023. OpenFOAM-Hybrid: A morphology adaptive multifield two-fluid model. Nucl. Sci. Eng. 197 (10), 2620–2633. http://dx.doi.org/10.1080/00295639.2022.2120316.

Štrubelj, L., Tiselj, I., 2011. Two-fluid model with interface sharpening. Internat. J. Numer. Methods Engrg. 85 (5), 575–590. http://dx.doi.org/10.1002/nme.2978.

Tekavčič, M., Meller, R., Schlegel, F., 2021. Validation of a morphology adaptive multi-field two-fluid model considering counter-current stratified flow with interfacial turbulence damping. Nucl. Eng. Des. 379, 111223. http://dx.doi.org/10.1016/j.nucengdes.2021.111223.

The OpenFOAM Foundation Ltd, OpenFOAM-dev, commit 3805586, July 27th 2022.

Tomiyama, A., Tamai, H., Zun, I., Hosokawa, S., 2002. Transverse migration of single bubbles in simple shear flows. Chem. Eng. Sci. 57 (11), 1849–1858. http://dx.doi.org/10.1016/S0009-2509(02)00085-4.

Wang, L.-S., Krull, B., Lucas, D., Meller, R., Schlegel, F., Tekavčič, M., Xu, J.-Y., 2023. Simulation of droplet entrainment in annular flow with a morphology adaptive multifield two-fluid model. Phys. Fluids 35 (10), http://dx.doi.org/10.1063/5.0169288.

Weller, H.G., 2008. A New Approach to VOF-based Interface Capturing Methods for Incompressible and Compressible Flow. Report TR/HGW 4, OpenCFD Ltd.